Journal of Nuclear Materials 557 (2021) 153262

Contents lists available at ScienceDirect

Journal of Nuclear Materials

journal homepage: www.elsevier.com/locate/jnucmat

The pores evolution in 3D view of nuclear graphite under ion beam irradiation

Fanggang Liu[a], Zhoutong He[a,*], Yu Wang[a], Yongqi Zhu[a], Bo huang[a], Alex Theodosiou[b], Andy Smith[c], Abbie Jones[b], Barry Marsden[b], Jianqiang Wang[a], Xingtai Zhou[a]

[a] Shanghai Institute of Applied Physics, Chinese Academy of Sciences, Shanghai 201800, PR China
[b] Nuclear Graphite Research Group, Department of MACE, The University of Manchester, M13 9LP, UK
[c] Dalton Cumbrian Facility, The University of Manchester, Westlakes Science & Technology Park, Moor Row, Cumbria CA24 3HA, UK

ARTICLE INFO

Article history:
Received 4 June 2021
Revised 18 August 2021
Accepted 19 August 2021
Available online 24 August 2021

Keywords:
Ion beam irradiation
Nuclear graphite
FIB-SEM tomography
Microcracks

ABSTRACT

As an outstanding material for moderator and reflector, graphite is broadly applied in nuclear reactors. Irradiation will change the pore structure and content, which is intimately related to the properties of graphite. However, the irradiation effect of nuclear graphite on pores requires a more profound understanding, especially the evolution on a three-dimensional(3D) view. In this work, FIB-SEM tomography intuitively reveal the pore structure and porosity evolution of ion irradiated graphite grades IG110 in a 3D view, which was irradiated with 30 MeV Ni^{5+} ion at 400 °C. Besides, the quantitative statistic of porosity indicates a negative correlation between porosity with the ion irradiation damage and confirms the consistency of ion deposition sites and irradiation damage peak. Moreover, individual microcracks of the different ion irradiated depths and virgin graphite are extracted and displayed in various 3D perspectives, which exhibit a much more complex morphology than lenticular structure and demonstrates the closed trend of the microcracks under irradiation. Through the display of 3D pore structure and quantitative statistics of porosity, aims to provide a further understanding of ion irradiation behavior of nuclear graphite.

1. Introduction

Due to the high neutron moderation ratio, high-temperature resistance, and exceptionally good chemical compatibility, nuclear graphite is widely used as moderator and reflector in various types of fission reactors [1–3]. Nuclear graphite is porous [4–6], and the properties of nuclear graphite, such as thermal conductivity, electrical conductivity, modulus, and CTE are intimately related to its porosity, pore size, connectivity, and morphology [7]. The pores also control the generation and propagation of cracks in graphite, which is highly related to the mechanical strength of the graphite [8]. Moreover, the pores in graphite, especially the microcracks, which are also referred to as Mrozowski cracks, are believed to be related to the irradiation-induced dimensional change, since the pores accommodate the swelling of the graphite crystal in c-axis direction [9, 10].

Since pores are critical to the performance of nuclear graphite, extensive research methods have been carried out on the pore of nuclear graphite. For example, the mercury intrusion [5,6] and nitrogen adsorption methods [11–13] are frequently applied in the study on the oxidation behavior of the nuclear graphite in gas-cooled reactors and molten salt reactor. The porosity of nuclear graphite was also characterized with X-ray and neutron beam small-angle scattering [14,15], and X-ray 3D tomography, which are capable of characterizing both the open and close pores. The microscopic observation methods, such as optical microscopy, SEM, TEM, etc., are also used to identify the characteristics of nuclear graphite and observe the evolution of the pores under various conditions (irradiation [11,16], loading [17], and oxidation [18]). However, the pore structure of nuclear graphite is far more than well understood. For instance, the microcrack is wildly believed to be lenticular shaped closed pore [10,19], observed by TEM. However, apart from TEM, there is little information about the evolution of the microcracks induced by irradiation on a 3D scale, which limits our intuitive understanding of the evolution of microcracks.

The characterization of microcracks evolution under irradiation is essential to understand the irradiation behaviors of a nuclear graphite [16]. Due to the low accessibility, highly expensiveness, and time-consuming of the fast neutron irradiation, ion beam irradiation as a surrogate to the fast neutron irradiation has been used to study the microstructure evolution of nuclear graphite under irradiation [16]. Again, most of the characterization of

* Corresponding author.
E-mail address: hezhoutong@sinap.ac.cn (Z. He).

https://doi.org/10.1016/j.jnucmat.2021.153262
0022-3115/

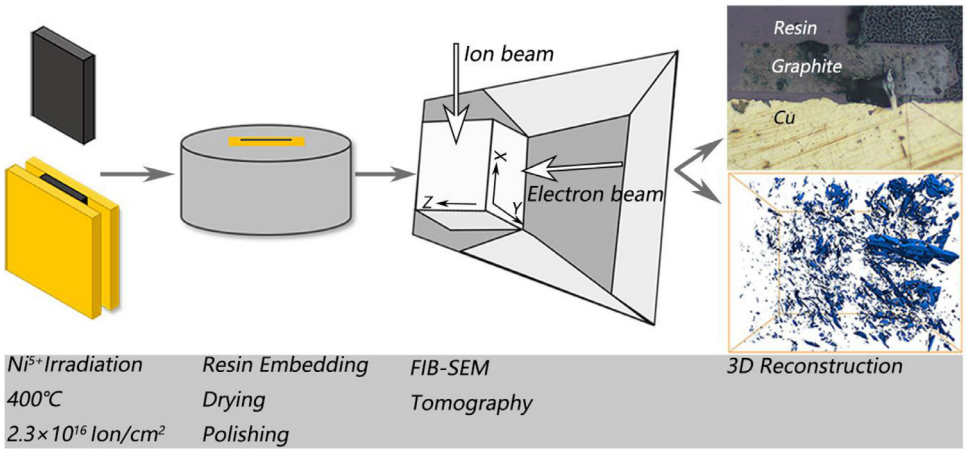

Fig. 1. Schematic diagram of sample preparation and characterization.

microcracks stays on the 2D level, and the 3D scale should be further advanced.

FIB-SEM tomography is a powerful technique for characterizing the microstructure in 3D view, which has been intensively used in earth science, biological science, and material science [20–22]. The microstructure characterization of graphite with FIB-SEM tomography has also been applied in many research fields. For example, Lin et al. used FIB-SEM to investigate the structure degradation behavior of commercial Lithium-ion battery graphite anodes [23], revealing that stress induced during lithiation and de-lithiation causes cracks to be the reason for degradation the graphite. Arregui-Mena et al. used FIB-SEM to characterize the pores in both the filler and binder areas of AGX grade graphite [8], revealing the 3D pore structure in the graphite filler and binder. Seldom work about the 3D morphology of microcracks in graphite and its evolution under irradiation have been published, especially in a fine-grained graphite.

Herein, FIB-SEM tomography was used to characterize the pore structure and its evolution under irradiated both in 2D and 3D view, with the graphite sample irradiated with 30 MeV Ni^{5+} ion beams at 400 °C. The distribution of the implanted nickel and the irradiation-induced damage has been analyzed. The porosity profile of the irradiated sample has been compared with the damage profile induced by the ion beam irradiation. The 2D and 3D views of the individual microcracks at various depths within and beyond the ion irradiation range have been compared.

2. Material and methods

2.1. Sample preparation and image acquisition

The Schematic diagram of sample preparation and characterization is shown in Fig. 1. The fine-grained graphite grade IG110 (Toyo Tanso Co) was used in this study, which is isostatic-molded graphite with a density of 1.77 g cm^{-3}, a porosity of ~21%, a grain size of ~20 μm, and a pore throat size of ~2 μm. The graphite sample (4 × 2 × 0.04 mm)was irradiated with 30 MeV Ni^{5+} ion beams at the temperature of 400 °C and the fluence of 2.3 × 10^{16} ions cm^{-2}, which was carried out with the 5MV Pelletron at Dalton Cambria Facility (DCF), the University of Manchester [24]. Neutron irradiations produce more cascade collisions and deeper damage depths due to no electrical energy; while ion irradiation is limited by the interaction of electrons, the damage depth is relatively shallow. Increasing the weight and energy of irradiated ions can effectively improve the irradiation depth and efficiency of ion irradiation damage. At the same times, nuclear graphite used in reactors usually runs at a high temperature above 400 °C. To simulate neutron irradiation more efficiently and better, the Ni^{5+} and 400 °C irradiation condition were prioritized. After irradiation, the graphite sample was cropped into small piece(0.2 × 2 × 0.04 mm) and embedded in epoxy resin, to keep the graphite vertical during the resin curing process, two copper sheets were used to clamp the sample.

Serial-sectioning on specific regions using focused ion beam and scanning electron microscopy (FIB-SEM, Zeiss, Cross Beam 540) was carried out to study the pore characteristics of the sample, and Ga as ion source is used in serial-sectioning. Before the serial-sectioning, two protective layers of platinum were deposited, of which the first layer was placed at the area of interest, and the second layer was used to mill a fiduciary mark serving as reference during the imaging process. Trenches were milled around the area of interest to improve the imaging conditions and to reduce redeposition of material, which with a beam current of 7 nA and energy of 30 kV. The volume of the slice area is 13 × 10 × 10 μm^3, a total of 1301 serial images were taken by SEM with an acceleration voltage of 5 kV and an electron beam current of 30 pA. Digital 3D reconstructions of the SEM images and the analysis of the porosity were conducted with Avizo. Before the reconstruction, the original SEM images were aligned with the least-squares algorithm and sheared to correct the y-direction position. The vertical striping artifacts produced by the milling process are removed to avoid the over selected in the threshold segmentation process and affect the porosity. Since the difference of gray values between the pore and the graphite matrix, interactive thresholding is used to segment the pore with a 0–33 intensity range. To extract individual pores, Labeling tool are used to label all pores, then Arithmetic combined with Volume rendering to display the specific pore structure in 3D views. To reduce the connection between the pores, Separate Objects tool are used before Labeling. The resultant dimensions of the bounding box reconstruction volume are 13 × 10 × 10 μm^3.

2.2. Nickel and irradiation damage distribution characterization

An electron probe microanalyzer (EPMA, EPMA-1720) was employed to determine the distribution of nickel and to identify the ion range of the Ni^{5+} ion beam. A line scan across the sample and an area scan covered 40 × 30 μm^2 were carried out to determine the distribution of the implanted nickel. The measurement is at an acceleration voltage of 15 kV, a beam current of 50 nA, and a unit measurement time of 50 ms/point. The results of the measurements were given in characteristic X-ray intensities of an element (Ni and C).

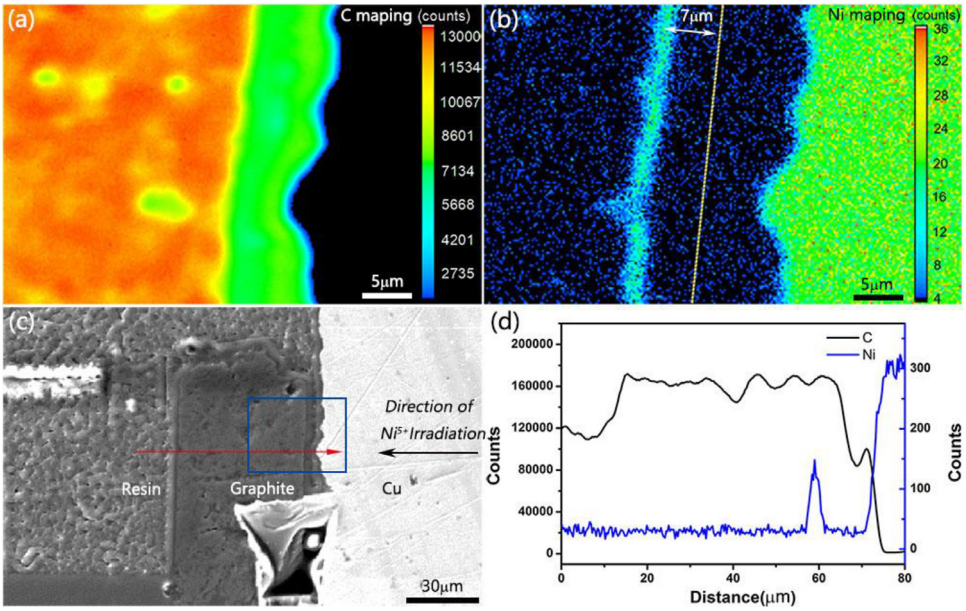

Fig. 2. The element distribution analysis of the Ni^{5+} ion beam irradiated sample with EPMA. (a) and (b) are the 2D element maps of C and Ni, respectively; (c) the position of line scan and surface scan acquired in the sample; (d) the element line scan of C and Ni (For interpretation of the references to color in this figure, the reader is referred to the web version of this article.).

Raman spectra were collected using an in Via Reflex microscope (Renishaw, confocal model) with a 532 nm laser, using a 5mW laser power and a 10 s acquisition time. 50 × objective lens was used to improve spatial resolution in the line scan and the Raman 2D maps. Cooperated with a micro-step XY stage, a spatial resolution of ~1 μm could be achieved in the Raman 2D maps.

2.3. Section polishing and SEM

Mechanical polishing is difficult to obtain a relatively flat surface, which will affect the quality of SEM imaging. To get the real structure of the pore and a good scanning electron microscope morphology, a three-ion beam cross-section cutter (Leica, TIC3X) is used to polish the cross-section of sample. Argon ions polished for 4 hours at an energy of 7 kV, and finally a flat area of 1 × 0.5 cm is formed around the sample.

The scanning electron microscope (SEM, Zeiss, Merlin compact) was used to observe the ion-polished cross section at a voltage of 8 kV, a working distance of 9.8 mm, a signal of SE2, and a magnification from 500 to 5000.

3. Results and discussions

3.1. The implanted nickel distribution

The sample was irradiated with 30 MeV Ni^{5+} ion beam at a fluence of 2.3 × 10^{16} ions cm^{-2}. The nickel distribution on the cross-section of the samples was measured with EPMA, as shown in Fig. 2. Fig. 2(a) and (b) are the 2D element maps of C and Ni on the cross-section of the sample, respectively. The area of the 2D element map acquired is marked by the blue rectangle in Fig. 2(c). The 2D element map of carbon shows a clear graphite and resin interface by the light-yellow line (Fig. 2(a)). The element map of nickel shows a distinct nickel enriched layer, and the layer is ~7 μm away from the graphite sample surface (yellow dotted line in Fig. 2(b)). And the thickness of nickel enriched layer is about 1.5 μm. The result of the element line scan of the carbon and nickel (Fig. 2(d)) is consistent with the result of the element 2D maps. As the damage induced by the ion beam irradiation is concentrated at the end of the ion trajectory, it can be deduced that the irradiation damage should be peaked ~ 7 μm depth. The incident Ni5+ ions induced defects in graphite while losing energy to the target atoms and stopping in the end, creating an implanted layer in the target. The energy loss of the 30 MeV Ni^{5+} ion in graphite, the induced damage, and the implanted ion profile were calculated with full-cascade TRIM simulation, which has a displacement energy of 28 eV. The displacement energy may be temperature-dependent, and McKenna et al. reported that the displacement energy should be 20 eV at room temperature and 35 eV at 900 K [25].

3.2. Irradiation damage distribution

Due to the sensitivity of the Raman spectroscopy to the defects in graphite [26,27] and the high spatial resolution of the micro Raman spectroscopy can be achieved, the profile of the damage induced by ion beam irradiation can be also characterized by Raman spectroscopy. Fig. 3(a) shows a typical SEM image of the sectioned sample, and the corresponding depths Raman spectra are shown in Fig. 3(b), which have been normalized by the G band height. As shown in Fig. 3(b), the Raman spectra of the sample at the depths of 1, 5, and 7 μm show typical Raman spectra of irradiated graphite, with a high D band (~1350 cm^{-1}), broad *G* band (~1580 cm^{-1}) and overlapped *D*' band (~1600 cm^{-1}). The Raman spectrum of the sample at the depth of 9 μm(unirradiated) shows a medium *D* band, sharp *G* band, and clear *D*' band, which are the characteristics of as-prepared artificial graphite. The *D* band of graphite is attributed to the defect or disorder in the graphitic lattice and always appears in artificial graphite, which is due to the inherent defects such as graphene edges, stacking disorder, etc. The intensity of the D band of the Raman spectrum at 7 μm is greater than those at 5 and 1 μm, and these three are greater than that at 9 μm. It indicates the sample at the depth of 9 μm is unaffected by the ion beam irradiation, also conflicting with the result of SRIM simulation.

To identify the depth of the irradiation damage peaked, Raman mapping has been conducted on the cross-section of the ion beam irradiated sample, shown in Fig. 3(c). The step size used is 1 μm,

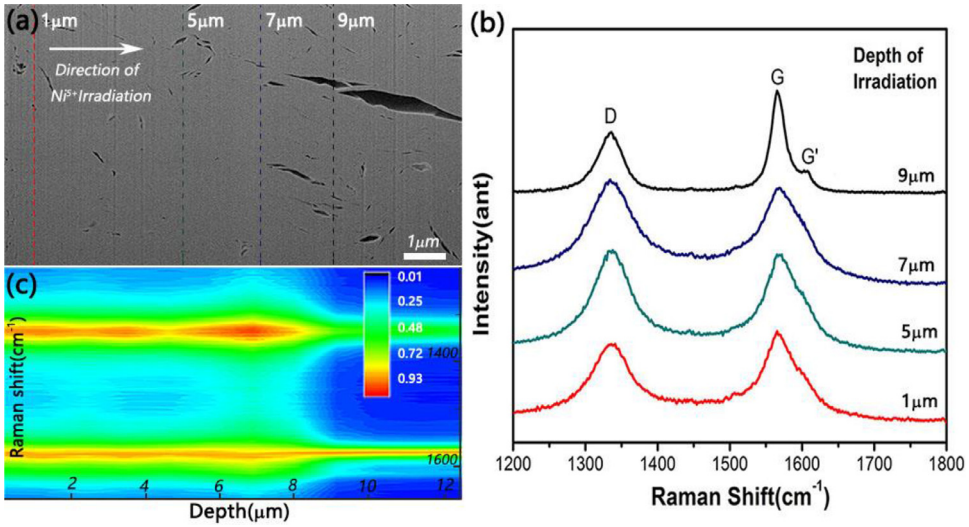

Fig. 3. The Raman spectra and Raman 2D maps of graphite sample. (a) a typical SEM image of the cross-section of the sample; (b) and (c) are the Raman spectra of the sample at different depths within and beyond the ion range.

and the intensity of the Raman spectra are normalized by the *G* band height. As shown in Fig. 3(c), the intensity of the *D* band, the width, and position of the *G* band change with depth within 8 μm, while those features keep unchanged at the depth beyond 8 μm. Because of the diameter of the laser spot used in the Raman spectrometer is about 1 μm, the irradiation-induced damage should be peaked at the depth between 7 and 8 μm, which is consistent with the nickel distribution measured by EPMA.

3.3. 3D visualization of pore structure

The 3D pore structure of the graphite sample has been investigated with the FIB-SEM tomography. Fig. 4 shows the 3D pore structure reconstructed from a different angle of view. Fig. 4(a) and (b) are the front view (*Z*-direction) and the top view (*Y*-direction) of the 3D pore distribution respectively, and the corresponding porosity statistics (Volume content) curve for depths. The ion beam enters the sample at the left of these two images. As shown in this 3D pore distribution and the porosity statistics curves, it can be noticed that there is a very distinct layer at the depth of about 7 μm, where the porosity is exceptionally low. According to the nickel distribution analyzed by the EPMA shown in Fig. 2 and the defects distribution analyzed by Raman spectroscopy shown in Fig. 3, it is assured that the irradiation induced damage peak is $\sim$ 7 μm beneath the sample surface, which matches the depth of the low porosity layer. Considering the sample was irradiated with 30 MeV Ni^{5+} ion beam at the fluence of 2.3×10^{16} ions cm^{-2}, the irradiation dose at the damage peak is $\sim$12 DPA, which is approaching to the turnaround dose of the irradiation dimensional change curve of IG110 at 400 °C [28]. It is believed that the turnaround of the graphite irradiation dimensional change curve is induced by the run out of the swelling absorption porosity [29]. The porosity of the position of 7 μm in depth may be partly consumed by the irradiation induced swelling. From the porosity statistics curve in Fig. 4(a), it can be note that the porosity within the ion irradiation range is lower ($\sim$3%), while that in the region beyond the ion irradiation range is much higher which is about 15%. Moreover, it can be observed that the pore size is much smaller in the near surface layer within the ion irradiation range than that in the region beyond the ion range.

Fig. 4(c) and (d) are the 3D visualizations of the pores in the sample at different visual angles, and they show the ion irradiation significantly changes the porosity of the sample.

3.4. 2D visualization of pore structure

To show the pore structure in more detail, the 2D visualization of the sample at various depth is shown in Fig. 5. Fig. 5(a) is the 2D pore structure of the sample view in Z-direction, and the irradiation ion enters the sample at the left of the image as labeled by the red arrow. Fig. 5(b–d) show the reconstructed 2D images of the sample at the depth of 1,7,9 μm, corresponding to the layers marked with the vertical red lines in Fig. 6(a), respectively. Fig. 5(b) and (c) are corresponding to the irradiated sample layer, among them, the sample region shown in Fig. 5(c) experienced the highest irradiation damage. Fig. 5(d) are corresponding to the graphite sample layers beyond the ion range. Both the 2D images of highly irradiation damaged layer (Fig. 5(c)) and the layers beyond the ion range (Fig. 5(d)) show a lot of lenticular cracks. However, it can be noticed that the microcracks shown in Fig. 5(c) are much narrower than those shown in Fig. 5(d), which explains the low porosity of the layer at the depth of $\sim$7 μm shown in Fig. 4. The length of the microcracks in these figures shows no remarkable difference. However, the microcracks in the irradiated layer have a significantly larger aspect ratio, which proved the closure of microcracks to accommodate to the swelling of graphite induced by irradiation [29].

3.5. SEM images of pore distribution

In view of the heterogeneous microstructure of IG-110 and the limitation of FIB-SEM observation scale ($13 \times 10 \times 10$ μm), to avoid the random variations in porosity distribution, a larger scale range of scanning electron microscope images of graphite along irradiation direction are presented in Fig. 6. To obtain a flat surface, ion beam cross-section cutting technology is used to process the sample cross-section. Fig. 6(c) is a low-magnification SEM image of graphite sample, Fig. 6(b) and (d) are high-magnification SEM micrographs of the red and blue rectangular area respectively, and Fig. 6(a) is the higher magnification SEM picture of Fig. 6(b). A field of view of 200×40 μm can be observed at the lowest magnification in Fig. 6(c), which is sufficient to avoid the random results of porosity distribution caused by graphite heterogeneous. There are obvious boundaries between the upper and lower parts of the graphite sample under SEM images with different magnifications. According to the measurement results, the distance from the boundary to the edge of the graphite is 7 μm, which is consistent with the results of EPMA and the 3D reconstruction of pores.

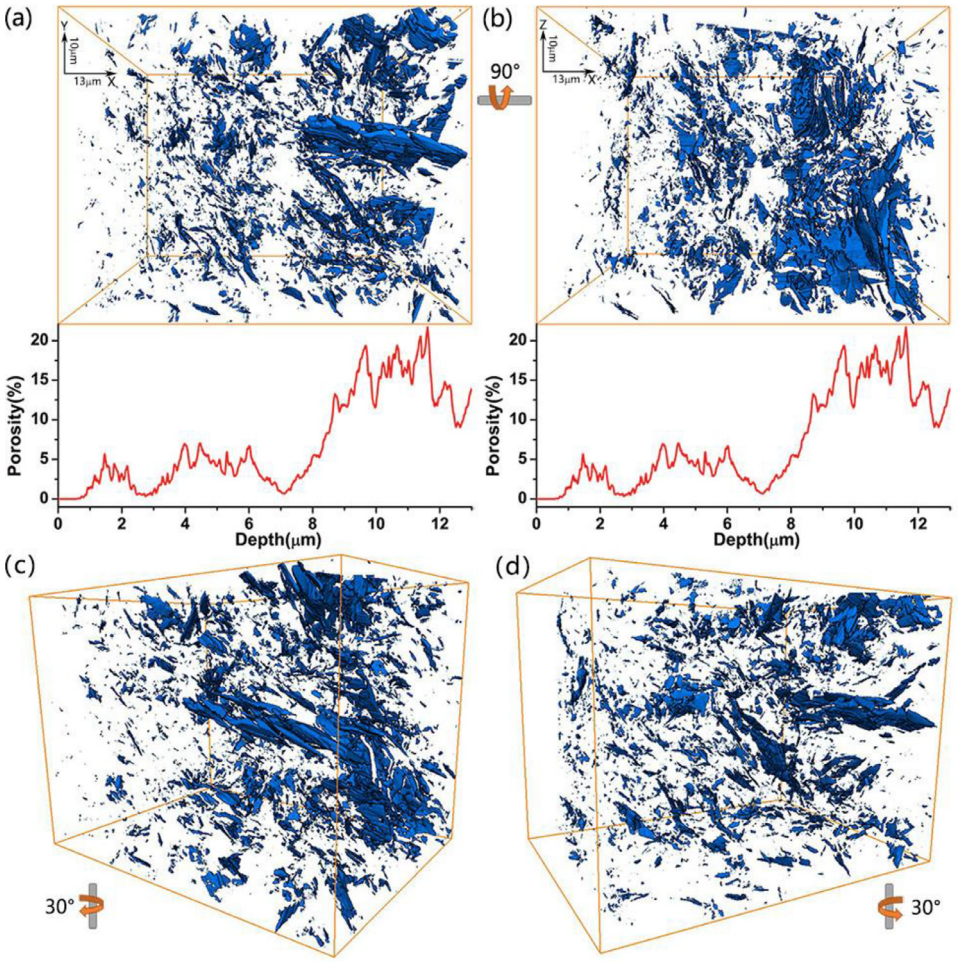

Fig. 4. The 3D visualization of the pore structure from different perspectives reconstructed from FIB-SEM tomography image dataset, and the corresponding porosity distribution with the depths. (a) and (b) are the front view (*Z* direction) and the top view (*Y* direction) of the 3D pore distribution respectively, and the corresponding porosity (Volume content) porosity statistics curve for depths; (c) and (d) are the angles of view rotated 30 degrees clockwise and counterclockwise with respect to the *Y*-axis from the front view, respectively.

At the same time, because of the pore distribution, there is a clear difference between the pore content of the irradiated area and the unirradiated area. From the microcrack1 and microcrack2 marked in Fig. 6(a), it can be seen that the extension of the microcracks is interrupted and closed where the irradiation damage peaked at 7 μm.

As we know, Mechanical processing will form stresses near the graphite surface, and the stresses and the mechanical processing will cause changes in the size and content of graphite pores. There is a dual effect of stress and mechanical landfill in the 14μm range near the surface. Benjamin März et al. studied the structural changes and residual stress induced by machining and polishing of a isostatic graphite, [30] concluded that the effect of machining on the near surface of graphite is mainly within depth of 40μm: near the top surface with a thickness of ~14 μm, large pores were filled with graphite fragments; inside a depth up to ~35–40 μm, graphite crystallites were refined by the machining operation. Due to area near the surface of 7–14 μm and the area of 0–7 μm have a significant difference in porosity, the significant decrease in porosity around 0–7 μm is mainly induced by irradiation.

3.6. 3D visualization of the individual microcracks

In Fig. 7, some typical microcracks at both the areas unaffected and affected by the irradiation are 3D visualized. Fig. 7(a) is the SEM image of the unirradiated region and the 3D visualization of the chosen microcracks. It shows several typical microcracks, and the corresponding 3D magnified, and rotated image are shown in Fig. 7(b). The microcracks shown in the SEM image are lenticular, however, the 3D views of the cracks are far from lenticular. Most of the microcracks are fragmented, with irregular rims and rough surfaces.

It is believed that the microcracks result from the anisotropic shrinkage of graphite crystallites as its cools from high temperature. The microcracks are imagined as a lenticular pore embedded in a graphite crystallite with an approximate circular out shape and smooth surface. While that is not the necessarily case from Fig. 7(b). The fragment and curling of the microcracks in graphite are reasonable, as graphite has a lamellar structure with the pliable and tough graphite plane. Generally, the graphite planes in an artificial graphite are usually curled, fragmented, which is evidenced by the TEM observation [10] and hinted by the small coherence length in both the a-axis and *c*-axis direction in X-ray diffraction characterization [4]. The microcracks sandwiched between the graphite planes would not be flat. Also, the microcracks may extent to different graphite plane stacks, which make the shape more complicate.

Fig. 7(c) is the SEM and 3D visualization image of the irradiated region, while Fig. 7(d) is the magnified and rotated 3D structure of the microcracks. From Fig. 7(c), the size of the microcracks is significantly smaller and the shape is more irregular than those in unirradiated region. In addition, compared with Fig. 7(b),

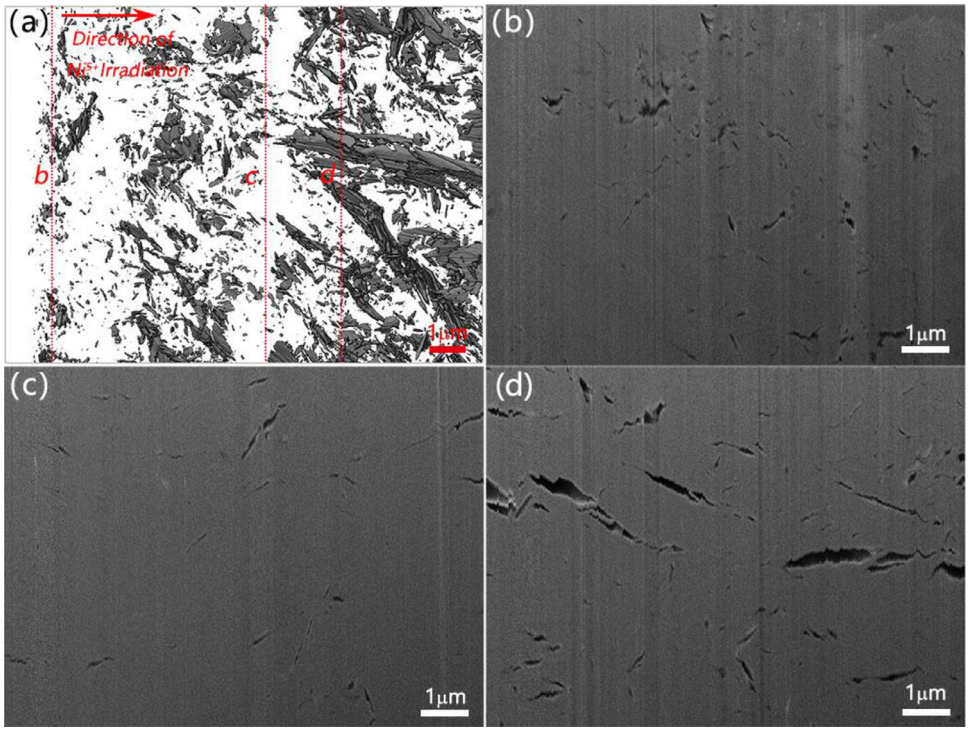

Fig. 5. The SEM images of graphite with various irradiation depths. (a) the 2D pore structure view in *Z*-direction; (b)–(d) are the 2D visualization of the reconstructed sample at the positions of 1,7,9 μm in depth, respectively.

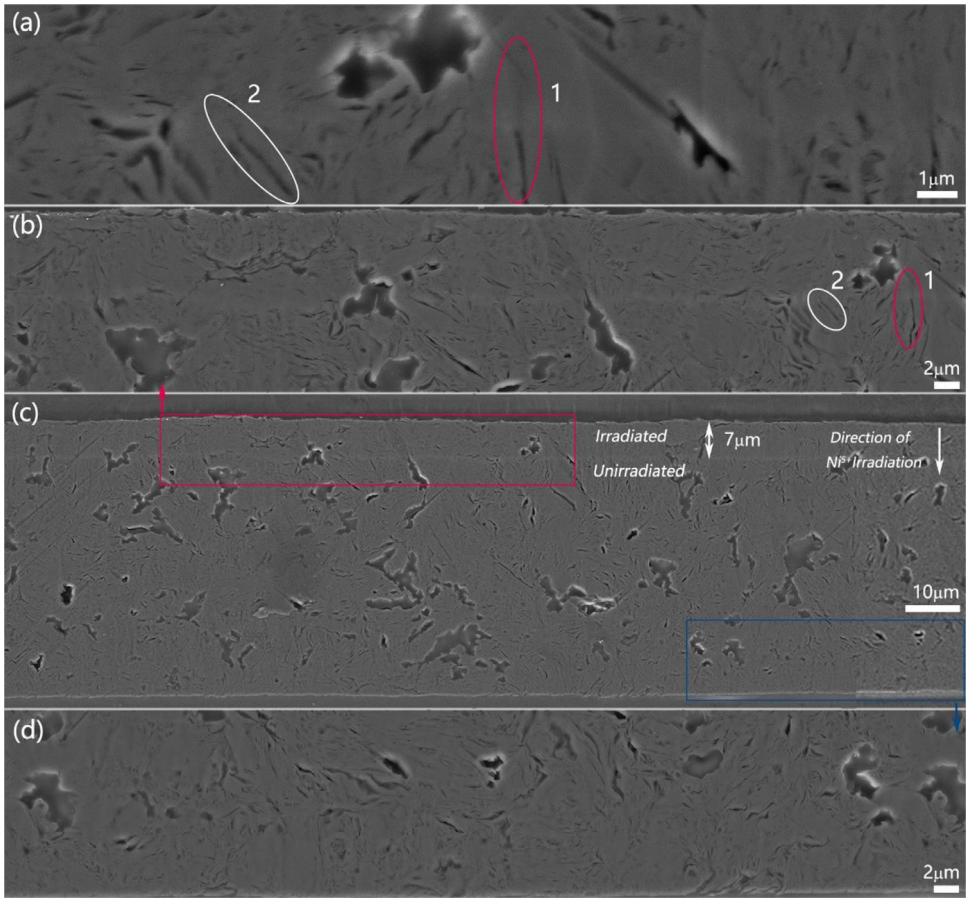

Fig. 6. The SEM images along the ion beam irradiation direction with different magnifications (For interpretation of the references to color in this figure, the reader is referred to the web version of this article.).

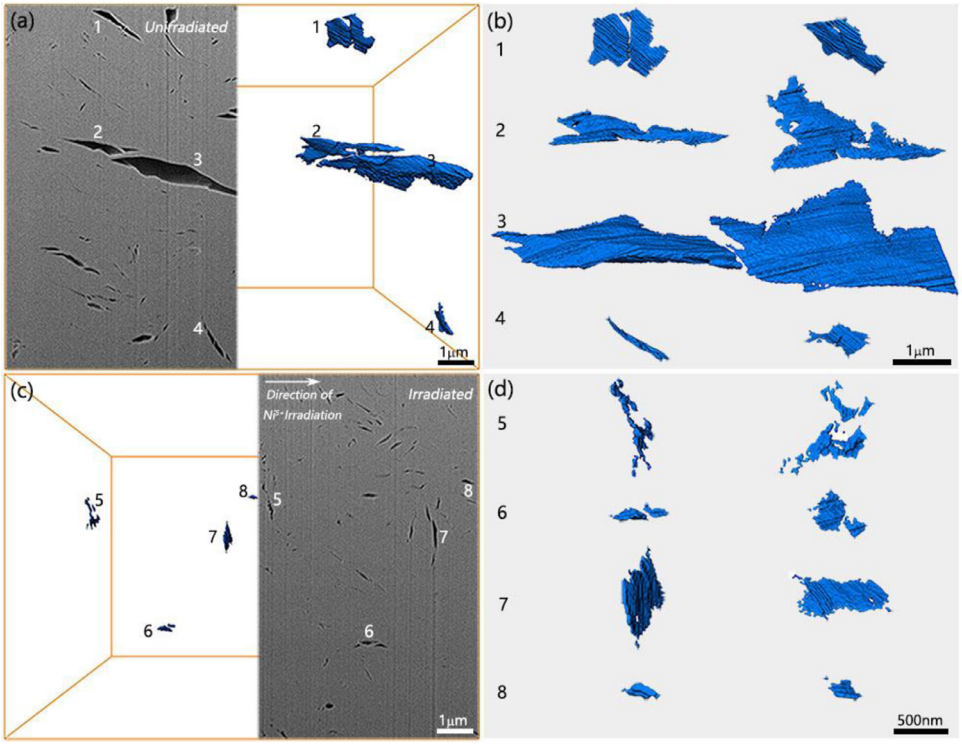

Fig. 7. The 3D visualization of the individual microcracks at the depths within and beyond ion irradiation range. (a) SEM image of the unirradiated region and the 3D visualization of the typical microcracks; (b) Magnified and rotated 3D visualization of the individual microcracks shown in Fig. 7 (a); (c) SEM image of the irradiated region and the 3D visualization of the typical microcracks; (d) Magnified and rotated 3D visualization of the individual microcracks shown in Fig. 7 (c).

the microcracks in Fig. 7(d) have a larger aspect ratio and more fragmented with intermittent connections, which demonstrates the closure of microcracks induced by irradiation that observed in the 3D level.

4. Conclusions

In summary, the graphite grades IG110 irradiated with 30 MeV Ni^{5+} ion at 400 °Cwas characterized by FIB-SEM tomography to reveal the pores evolution induced by irradiation in 3D scale. Both the nickel distribution by the EPMA and the structure analysis by the Raman spectroscopy indicate the irradiation damage was peaked at ~7 μm depth, and quantitative statistics of the porosity combined with 3D reconstruction of the pores demonstrate the strict correspondence between radiation damage peak and ion deposition sites. The 3D perspectives of individual microcracks with different irradiation depths and virgin graphite show off the closure of microcracks induced by irradiation, which is quite different from the lenticular structure recognized by previous scholars. Through the characterization of ion-irradiated graphite, aimed at a more intuitive cognition of graphite irradiation behavior at a 3D scale.

Declaration of Competing Interest

The authors declare that they have no known competing financial interests or personal relationships that could have appeared to influence the work reported in this paper.

The authors declare the following financial interests/personal relationships which may be considered as potential competing interests.

CRediT authorship contribution statement

Fanggang Liu: Data curation, Visualization, Writing – original draft, Conceptualization, Software, Writing – review & editing. **Zhoutong He:** Methodology, Supervision, Writing – review & editing. **Yu Wang:** Software. **Yongqi Zhu:** Formal analysis. **Bo huang:** Validation. **Alex Theodosiou:** Methodology. **Andy Smith:** Writing – review & editing. **Abbie Jones:** Writing – review & editing. **Barry Marsden:** Methodology. **Jianqiang Wang:** Writing – review & editing. **Xingtai Zhou:** Writing – review & editing.

Acknowledgments

This work supported by the National Key Research and Development Program of China (No. 2017YFA0402800), the Natural Science Foundation of Shanghai (No.19ZR1468100), and the National Natural Science Foundation of China (No. 11305240). The authors also acknowledge the support of The University of Manchester's Dalton Cumbrian Facility (DCF), a partner in the National Nuclear User Facility, the EPSRC UK National Ion Beam Centre and the Henry Royce Institute and thank the staff at DCF for helping with the ion beam irradiation. The authors thank beamline BL14B1 staff at SSRF and User Experiment Assist System of SSRF for their help.

References

[1] W.P. Eatherly, Nuclear graphite-the first years, J. Nucl. Mater. 100 (1) (1981) 55–63.
[2] B. McEnaney, CHAPTER 1-structure and bonding in carbon materials, in: T.D. Burchell (Ed.), Carbon Materials for Advanced Technologies, Elsevier Science Ltd, Oxford, 1999, pp. 1–33.
[3] R.E. Nightingale, CHAPTER ONE-graphite in the nuclear industry, in: R.E. Nightingale (Ed.), Nuclear Graphite, Academic Press2013, pp. 1-20.
[4] Z. He, L. Gao, X. Wang, B. Zhang, W. Qi, J. Song, X. He, C. Zhang, H. Tang, H. Xia, Improvement of stacking order in graphite by molten fluoride salt infiltration, Carbon 72 (2014) 304–311.

[5] H. Tang, W. Qi, Z. He, H. Xia, Q. Huang, C. Zhang, X. Wang, J. Song, P. Huai, X. Zhou, Infiltration of graphite by molten 2LiF–BeF 2 salt, J. Mater. Sci. 52 (19) (2017) 11346–11359.
[6] Z. He, L. Gao, W. Qi, B. Zhang, X. Wang, J. Song, X. He, C. Zhang, H. Tang, R. Holmes, Molten FLiNaK salt infiltration into degassed nuclear graphite under inert gas pressure, Carbon 84 (2015) 511–518.
[7] P. Delhaes, Graphite and precursors, CRC Press2000.
[8] J.D. Arregui-Mena, P.D. Edmondson, A.A. Campbell, Y. Katoh, Site specific, high--resolution characterisation of porosity in graphite using FIB-SEM tomography, J. Nucl. Mater. 511 (2018) 164–173.
[9] J.H.W. Simmons, Chapter 5-the effect of irradiation on the thermal and structural properties of graphite, in: J.H.W. Simmons (Ed.), Radiation Damage in Graphite, Pergamon, 1965, pp. 102–135.
[10] K. Wen, J. Marrow, B. Marsden, Microcracks in nuclear graphite and highly oriented pyrolytic graphite (HOPG), J. Nucl. Mater. 381 (1-2) (2008) 199–203.
[11] C.I. Contescu, J.D. Arregui-Mena, A.A. Campbell, P.D. Edmondson, N.C. Gallego, K. Takizawa, Y. Katoh, Development of mesopores in superfine grain graphite neutron-irradiated at high fluence, Carbon 141 (2019) 663–675.
[12] K.L. Jones, G.M. Laudone, G.P. Matthews, A multi-technique experimental and modeling study of the porous structure of IG-110 and IG-430 nuclear graphite, Carbon 128 (2018) 1–11.
[13] C.I. Contescu, T. Guldan, P. Wang, T.D. Burchell, The effect of microstructure on air oxidation resistance of nuclear graphite, Carbon 50 (9) (2012) 3354–3366.
[14] Z. Mileeva, D. Ross, S. King, A study of the porosity of nuclear graphite using small-angle neutron scattering, Carbon 64 (2013) 20–26.
[15] Z. Zhou, W.G. Bouwman, H. Schut, S. Desert, J. Jestin, S. Hartmann, C. Pappas, From nanopores to macropores: Fractal morphology of graphite, Carbon 96 (2016) 541–547.
[16] C. Karthik, J. Kane, D.P. Butt, W.E. Windes, R. Ubic, In situ transmission electron microscopy of electron-beam induced damage process in nuclear grade graphite, J. Nucl. Mater. 412 (3) (2011) 321–326.
[17] J.E.L. Taylor, G.N. Hall, P.M. Mummery, Investigating the effects of stress on the pore structures of nuclear grade graphites, J. Nucl. Mater. 470 (2016) 216–228.
[18] P. Wang, C.I. Contescu, S. Yu, T.D. Burchell, Pore structure development in oxidized IG-110 nuclear graphite, J. Nucl. Mater. 430 (1) (2012) 229–238.
[19] H.M. Freeman, A.N. Jones, M.B. Ward, F.S. Hage, N. Tzelepi, Q.M. Ramasse, A.J. Scott, R.M.D. Brydson, On the nature of cracks and voids in nuclear graphite, Carbon 103 (2016) 45–55.
[20] B. Bera, S.K. Mitra, D. Vick, Understanding the micro structure of Berea Sandstone by the simultaneous use of micro-computed tomography (micro-CT) and focused ion beam-scanning electron microscopy (FIB-SEM), Micron 42 (5) (2011) 412–418.
[21] D. Cretoiu, E. Hummel, H. Zimmermann, M. Gherghiceanu, L.M. Popescu, Human cardiac telocytes: 3D imaging by FIB-SEM tomography, J. Cell Mol. Med. 18 (11) (2014) 2157–2164.
[22] A. Bordes, E. De Vito, C. Haon, C. Secouard, A. Montani, P. Marcus, Investigation of lithium insertion mechanisms of a thin-film si electrode by coupling time-of-flight secondary-ion mass spectrometry, X-ray photoelectron spectroscopy, and focused-ion-beam/SEM, ACS Appl. Mater. Interfaces 7 (50) (2015) 27853–27862.
[23] N. Lin, Z. Jia, Z. Wang, H. Zhao, G. Ai, X. Song, Y. Bai, V. Battaglia, C. Sun, J. Qiao, K. Wu, G. Liu, Understanding the crack formation of graphite particles in cycled commercial lithium-ion batteries by focused ion beam - scanning electron microscopy, J. Power Sources 365 (2017) 235–239.
[24] L. Leay, W. Bower, G. Horne, P. Wady, A. Baidak, M. Pottinger, M. Nancekievill, A.D. Smith, S. Watson, P.R. Green, B. Lennox, J.A. LaVerne, S.M. Pimblott, Development of irradiation capabilities to address the challenges of the nuclear industry, Nucl. Instrum. Methods Phys. Res. Sect. B Beam Interact. Mater. Atoms 343 (2015) 62–69.
[25] A.J. McKenna, T. Trevethan, C.D. Latham, P.J. Young, M.I. Heggie, Threshold displacement energy and damage function in graphite from molecular dynamics, Carbon 99 (2016) 71–78.
[26] Z. He, H. Xia, X. Zhou, X. Yang, Y. Song, T. Wang, Raman study of correlation between defects and ferromagnetism in graphite, J. Phys. D Appl. Phys. 44 (8) (2011) 085001.
[27] S. Reich, C. Thomsen, Raman spectroscopy of graphite, philosophical transactions of the royal society of London, Ser. A Math. Phys. Eng. Sci. 362 (1824) (2004) 2271–2288.
[28] S. Ishiyama, T.D. Burchell, J.P. Strizak, M. Eto, The effect of high fluence neutron irradiation on the properties of a fine-grained isotropic nuclear graphite, J. Nucl. Mater. 230 (1) (1996) 1–7.
[29] B.T. Kelly, Physics of graphite (1981).
[30] B. März, K. Jolley, R. Smith, H. Wu, Near-surface structure and residual stress in as-machined synthetic graphite, Mater. Des. 159 (2018) 103–116.